Hierarchical Anatomical Brain Networks for MCI Prediction: Revisiting Volumetric Measures

Luping Zhou[1], Yaping Wang[1], Yang Li[1], Pew-Thian Yap[1], Dinggang Shen[1]*, and the Alzheimer's Disease Neuroimaging Initiative (ADNI)[2]

1 IDEA Lab, Department of Radiology and BRIC, University of North Carolina, Chapel Hill, North Carolina, United States of America, 2 Alzheimer's Disease Neuroimaging Initiative, Department of Neurology, University of California Los Angeles, Los Angeles, California, United States of America

Abstract

Owning to its clinical accessibility, T1-weighted MRI (Magnetic Resonance Imaging) has been extensively studied in the past decades for prediction of Alzheimer's disease (AD) and mild cognitive impairment (MCI). The volumes of gray matter (GM), white matter (WM) and cerebrospinal fluid (CSF) are the most commonly used measurements, resulting in many successful applications. It has been widely observed that disease-induced structural changes may not occur at isolated spots, but in several inter-related regions. Therefore, for better characterization of brain pathology, we propose in this paper a means to extract inter-regional correlation based features from local volumetric measurements. Specifically, our approach involves constructing an anatomical brain network for each subject, with each node representing a Region of Interest (ROI) and each edge representing Pearson correlation of tissue volumetric measurements between ROI pairs. As second order volumetric measurements, network features are more descriptive but also more sensitive to noise. To overcome this limitation, a hierarchy of ROIs is used to suppress noise at different scales. Pairwise interactions are considered not only for ROIs with the same scale in the same layer of the hierarchy, but also for ROIs across different scales in different layers. To address the high dimensionality problem resulting from the large number of network features, a supervised dimensionality reduction method is further employed to embed a selected subset of features into a low dimensional feature space, while at the same time preserving discriminative information. We demonstrate with experimental results the efficacy of this embedding strategy in comparison with some other commonly used approaches. In addition, although the proposed method can be easily generalized to incorporate other metrics of regional similarities, the benefits of using Pearson correlation in our application are reinforced by the experimental results. Without requiring new sources of information, our proposed approach improves the accuracy of MCI prediction from 80.83% (of conventional volumetric features) to 84.35% (of hierarchical network features), evaluated using data sets randomly drawn from the ADNI (Alzheimer's Disease Neuroimaging Initiative) dataset.

Introduction

Alzheimer's disease (AD) is a progressive and eventually fatal disease of the brain, characterized by memory failure and degeneration of other cognitive functions. Pathology may begin long before the patient experiences any symptom and often lead to structural changes of brain anatomies. With the aid of medical imaging techniques, it is now possible to study in vivo the relationship between brain structural changes and the mental disorder, providing a diagnosis tool for early detection of AD. Current studies focus on MCI (mild cognitive impairment), a transitional state between normal aging and AD. These subjects suffer from memory impairment that is greater than expected for their age, but retain general cognitive functions to maintain daily living. Identifying MCI subjects is important, especially for those that will eventually convert to AD (referred to as Progressive-MCI, or in short P-MCI), because they may benefit from therapies that could slow down the disease progression.

Although T1-weighted MRI, as a diagnostic tool, is relatively well studied, it continues to receive the attention of researchers due to its easy access in clinical settings, compared with task-based functional imaging [1]. Commonly used measurements can be categorized into three groups: regional brain volumes [1–7], cortical thickness [8–12] and hippocampal volume and shape [13–15]. Volumetric measurements can be further divided into two groups according to feature types: voxel-based features [16] or region-based features [17,18]. In this paper, we focus on region-based volumetric measurements of the whole brain for the following reasons. Firstly, the abnormalities caused by the disease involved in our study are not restricted to the cortex, because, as shown by pathological studies [19], AD related atrophy begins in the medial temporal lobe (MTL), which includes some subcortical structures such as the hippocampus and the amygdala. Secondly, a whole brain analysis not restricted to the hippocampus is preferred, because early-stage AD pathology is not confined to the hippocampus. Also affected are the entorhinal cortex, the amygdala, the limbic system, and the neocortical areas. As has been pointed out in several studies [1,20], although the analysis of the earliest-affected structures, such as the hippocampus and the entorhinal cortex, can increase the sensitivity of MCI prediction,

the inclusion of the later-affected temporal neocortex may increase the prediction specificity, and hence improve the overall classification accuracy [20]. Thirdly, we focus on region-based volumetric features because voxel-based features are highly redundant [21], which may affect their discrimination power.

The determination of the Region of Interest (ROI) is the key for region-based analysis methods. Once ROIs have been determined either by pre-definition [17,18] or by adaptive parcellation [4,5,21], the mean tissue densities of gray matter (GM), white matter (WM) and cerebrospinal fluid (CSF) in each ROI are usually used as features for classification. Disease-induced brain structural changes may occur not at isolated spots, but in several inter-related regions. Therefore, for a more accurate characterization of the pathology, feature correlation between ROIs has to be taken into account. Measurement of such correlations may provide potential biomarkers associated with the pathology, and hence is of great research interest. However, for most existing approaches, the dependencies among features are not explicitly modelled in the feature extraction procedure, but only implicitly considered by some classifiers, such as the support vector machines (SVMs), during the classification process. For example, a linear SVM classifier models the dependency (inner product) of feature vectors between two subjects, instead of the interaction of two ROIs (via volumetric features) of a specific subject. These implicitly encoded feature dependencies become more difficult to interpret when a nonlinear SVM classifier is used. Based on this observation, we propose in this paper a new type of features derived from regional volumetric measurements, by taking into account the pairwise ROI interactions within a subject directly. To achieve this, each ROI is first characterized by a vector that consists of the volumetric ratios of GM, WM and CSF in this ROI. Then, the interaction between two ROIs within the same subject is computed as Pearson correlation of the corresponding volumetric elements. This gives us an anatomical brain network, with each node denoting an ROI and each edge characterizing the pairwise connection.

The correlation value measures the similarity of the tissue compositions between a pair of brain regions. When a patient is affected by MCI, the correlation values of a particular brain region with another region will be potentially affected, due possibly to the factors such as tissue atrophy. These correlation changes will be finally captured by classifiers and used for MCI prediction. An early work was presented in a conference [22]. It is worth noting that by computing the pairwise correlation between ROIs, our approach provides a second order measurement of the ROI volumes, in contrast to the conventional approaches that only employ first order volumetric measurement. As higher order measurements, our new features may be more descriptive, but also more sensitive to noise. For instance, the influence of a small ROI registration error may be exaggerated by the proposed network features, which may reduce the discrimination power of the features. To overcome this problem, a hierarchy of multi-resolution ROIs is used to increase the robustness of classification. Effectively, the correlations are considered at different scales of regions, thus providing different levels of noise suppression and discriminative information, which can be sieved by a feature selection mechanism as discussed below for guiding the classification. Additionally, we consider the correlations both within and between different resolution scales. This is because the optimal scale is often not known a priori. We will demonstrate the effectiveness of the proposed approach with empirical evidence. In this study, we consider a fully-connected anatomical network, features extracted from which will form a space with intractably high dimensionality. As a remedy, a supervised dimensionality reduction method is employed to embed the original network features into a new feature space with a much lower dimensionality.

Without requiring any new information in addition to the baseline T1-weighted images, the proposed approach improves the prediction accuracy of MCI from 80.83% (of conventional volumetric features) to 84.35% (of hierarchical network features), evaluated by data sets randomly drawn from the ADNI dataset [23]. Our study shows that this improvement comes from the use of the network features obtained from hierarchical brain networks. To investigate the generalizability of the proposed approach, experiments are conducted repetitively based on different random partitions of training and test data sets with different partition ratios. The average classification accuracy estimated in this way tends to be more conservative than the conventional Leave-One-Out approach. Additionally, although the proposed approach can be easily generalized to incorporate regional similarity measurements other than Pearson correlation, the experimental results reinforce the choice of Pearson correlation for our application, compared with some commonly used similarity metrics.

Before introducing our proposed approach, it is worth highlighting the advantages of the hierarchical brain network-based approach over the conventional volume-based approaches. Firstly, as mentioned above, our proposed method utilizes a second-order volumetric measurement that is more descriptive than the conventional first-order volumetric measurement. Secondly, compared with the conventional volumetric measurements that only consider local volume changes, our proposed hierarchical brain network considers global information by pairing ROIs that may be spatially far away. Thirdly, our proposed method seamlessly incorporates both local volume features and global network features for the classification by introducing a whole-brain ROI at the top of the hierarchy. By correlating with the whole-brain ROI, each ROI can provide a first order measurement of local volume. Fourthly, although our current approach uses Pearson correlation, it can be easily generalized to any other metrics that are capable of measuring the similarity between features of ROI pairs. Fifthly, the proposed method involves only linear methods, leading to easy interpretations of the classification results. Finally, for the first time, we investigate the *relative* speeds of disease progression in different regions, providing a different pathological perspective complementary to spatial atrophy patterns.

Materials and Methods

Participants

Both the normal control and MCI subjects used in the preparation of this article were obtained from the Alzheimer's Disease Neuroimaging Initiative (ADNI) database (www.loni.ucla.edu/ADNI) [23]. The ADNI was launched in 2003 by the National Institute on Aging (NIA), the National Institute of Biomedical Imaging and Bioengineering (NIBIB), the Food and Drug Administration (FDA), private pharmaceutical companies and non-profit organizations as a 60 million, 5-year public private partnership. The primary goal of ADNI has been to test whether serial MRI, PET (Positron Emission Tomography), other biological markers, and clinical and neuropsychological assessment can be combined to measure the progression of MCI and early AD. Determination of sensitive and specific markers of very early AD progression is intended to aid researchers and clinicians in the development of new treatments and monitor their effectiveness, as well as lessen the time and cost of clinical trials. The image acquisition parameters have been described in www.adniinfo.org. The ADNI protocol included a sagittal volumetric 3D MPRAGE

with 1.25×1.25 mm in-plane spatial resolution and 1.2-mm thick sagittal slices (8 flip angle). TR and TE values of the ADNI protocol were somewhat variable, but the target values were TE 3.9 ms and TR 8.9 ms.

The ADNI data were previously collected across 50 research sites. Study subjects gave written informed consent at the time of enrollment for imaging and genetic sample collection and completed questionnaires approved by each participating sites Institutional Review Board (IRB). More information about the ADNI investigators is given in Acknowledgement.

In this study, 125 normal control subjects and 100 P-MCI subjects are taken from the ADNI dataset. Each subject is rescanned and re-evaluated every six months for up to 36 months. The P-MCI subjects are those who developed probable AD after the baseline scanning. The diagnosis of AD is made according to the NINCDS/ADRDA criteria [24] for probable AD. The demographic and clinical information of all the selected subjects are summarized in Table 1.

Image Preprocessing

The T1-weighted MR brain images are skull-stripped and cerebellum-removed after a correction of intensity inhomogeneity using N3 algorithm [25]. Then each MR brain image is further segmented into three tissue types, namely GM, WM, and CSF. To compare structural patterns across subjects, the tissue-segmented brain images are spatially normalized into a template space (called the stereotaxic space) by a mass-preserving registration framework proposed in [26]. During image warping, the tissue density within a region is increased if the region is compressed, and vice versa. These tissue density maps reflect the spatial distribution of tissues in a brain by taking into consideration the local tissue volume prior to warping. After spatial normalization, we can then measure the volumes of GM, WM, and CSF in each predefined ROI. More details about the ROI hierarchy are given in Section "Hierarchical ROI Construction".

Method Overview

The overview of the proposed method is illustrated in Fig. 1. Each brain image is parcellated in multi-resolution according to hierarchically predefined ROIs. The local volumes of GM, WM, and CSF are then measured within these ROIs and used to construct an anatomical brain network. Each node of the network represents an ROI, and each edge represents the correlation of local tissue volumes between two ROIs. The edge values (the correlations) are concatenated to form the feature vectors for use in classification. This gives rise to a large amount of features. For a robust classification, both feature selection and feature embedding algorithms are used to remove many noisy, irrelevant, and redundant features. Only essentially discriminative features are kept to train our classifier that can be well generalized to predict previously unseen subjects. In the following, the description of the proposed method is divided into

three parts: hierarchical ROI construction (Section "Hierarchical ROI Construction"), feature extraction (Section "Feature Extraction"), and classification (Section "Classification").

Hierarchical ROI Construction

In this paper, a four-layer ROI hierarchy is proposed to improve the classification performance of volumetric measurements. Each layer corresponds to a brain atlas with different resolution. To make the explanation of our method clear, the bottommost layer that contains the finest ROIs is denoted as $\mathcal{L}^4$, while the other three layers are denoted as $\mathcal{L}^l$, where $l = 1,2,3$. A smaller l denotes a coarser ROI which is in a layer closer to the top of the hierarchy. In our approach, the bottommost layer $\mathcal{L}^4$ contains 100 ROIs obtained according to [27]. These ROIs include fine cortical and subcortical structures, ventricle system, cerebellum, brainstem, etc. Note that in our case, the cerebellum and the brainstem are removed and the respective ROIs are not actually used. The number of ROIs reduces to 44 and 20, respectively, in the layers $\mathcal{L}^3$ and $\mathcal{L}^2$ by agglomerative merging of the 100 ROIs in the layer $\mathcal{L}^4$. In the layer $\mathcal{L}^3$, the cortical structures are grouped into frontal, parietal, occipital, temporal, limbic, and insula lobe in both left and right brain hemispheres. Each cortical ROI has three sub-ROIs, namely the superolateral, medial and white matter ROIs. The subcortical structures are merged into three groups in each hemisphere of the brain, namely, the basal ganglia, hippocampus and amygdala (including fornix), and diencephalon. Other ROIs include the ventricle and the corpus callosum. In the layer $\mathcal{L}^2$, the sub-groups of the superolateral, medial or white matter parts within each cortical ROI are merged together. All the subcortical ROIs are grouped into one ROI. Other ROIs remain the same in the layer $\mathcal{L}^2$ as in the layer $\mathcal{L}^3$. The topmost layer $\mathcal{L}^1$ contains only one ROI, the whole brain. This layer $\mathcal{L}^1$ is included because when correlated with the ROIs in $\mathcal{L}^4$, it gives us a measurement comparable to the original volumetric measurements, thus allowing us to also include the original volumetric features for classification. The ROIs for different layers are shown in Fig. 2 (a). The number of ROIs in each layer of the hierarchy is illustrated in Table 2.

Feature Extraction

With the ROI hierarchy defined above, an anatomical brain network can be constructed for each subject, from which informative features are extracted for classification. For each brain network, its nodes correspond to the brain ROIs, and its undirected edges correspond to the interactions between two ROIs. There are two types of nodes in our model (Fig. 2-left): the simple ROI in the bottommost layer $\mathcal{L}^4$, and the compound ROI in the other layers. Similarly, we have two types of edges, each modelling within-layer and between-layer ROI interactions, respectively (Fig. 3-right).

The brain network may be quite complicated. For instance, Fig. 2 (b) partially shows the network connections between ROIs in the layers of $\mathcal{L}^2$, $\mathcal{L}^3$ and $\mathcal{L}^4$, respectively. To determine informative features from the network, the computation of ROI interactions is initially conducted on the bottommost layer $\mathcal{L}^4$, and then propagated to other layers effectively via a membership matrix that indicates the relationship of ROIs from different layers. The process is detailed as follows.

Firstly, let us consider the bottommost layer $\mathcal{L}^4$, which consists of 100 ROIs. Let $\mathbf{f}_i$ denote the 3×1 vector of the i-th ROI in $\mathcal{L}^4$, consisting of the volumetric ratios of GM, WM, and CSF in that ROI. We can obtain an $N^4 \times N^4$ matrix $\mathbf{C}^4$, where N^4 is the number of ROIs in $\mathcal{L}^4$. The (i, j)-th component in $\mathbf{C}^4$ corresponds to the weight of the edge between the i-th node and the j-th node

Table 1. Demographic information of the subjects involved in the study.

	Normal Control	P-MCI
No. of Subjects	125	100
No. & Percentage of males	61(48.8%)	57(57%)
Baseline age, mean(STD)	76.1(5.1)	75.0(7.1)
Baseline MMSE, mean(STD)	29.1(1.0)	26.5(1.7)

doi:10.1371/journal.pone.0021935.t001
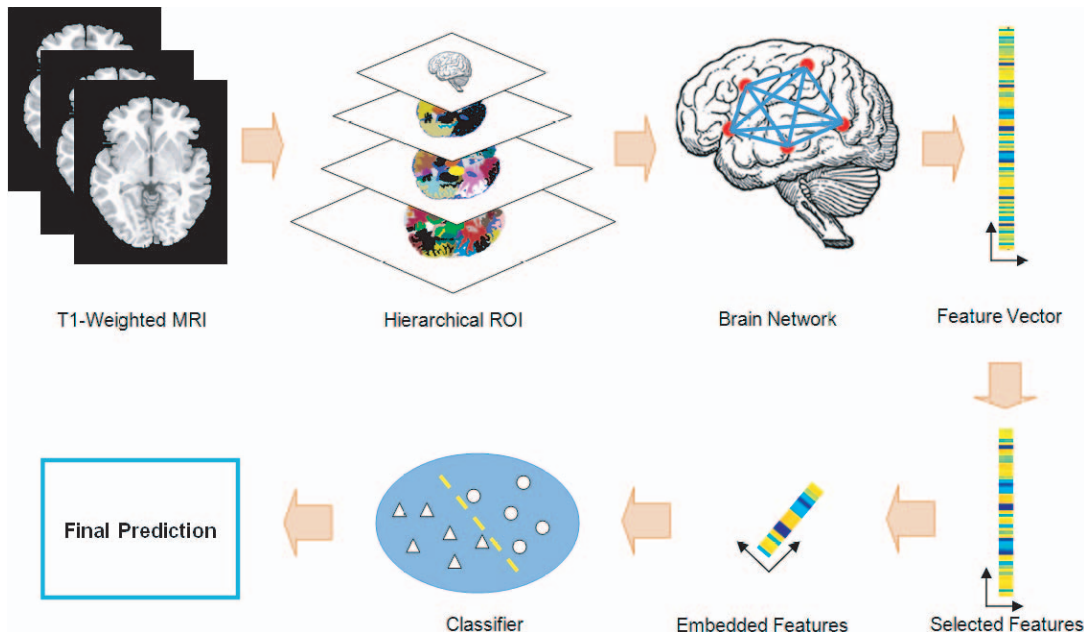
Figure 1. Overview of our proposed method.
doi:10.1371/journal.pone.0021935.g001

in $\mathcal{L}^4$. We define $\mathbf{C}^4(i,j) = corr(\mathbf{f}_i, \mathbf{f}_j)$, the Pearson correlation between feature vectors $\mathbf{f}_i$ and $\mathbf{f}_j$.

For any other layer $\mathcal{L}^l$, let R_i^l represent the i-th ROI in the layer $\mathcal{L}^l$. The number of ROIs in the layer $\mathcal{L}^l$ is denoted as N^l. A membership matrix $\mathbf{M}^l$ (Fig. 4) is used to define the composition of the compound ROI R_i^l in $\mathcal{L}^l$. The matrix $\mathbf{M}^l$ has N^l rows and N^4 columns. Each row corresponds to a single compound ROI in $\mathcal{L}^l$. Each column corresponds to a single simple ROI in $\mathcal{L}^4$. The (i,j)-th component of $\mathbf{M}^l$ takes the value of either 1 or 0, indicating whether the j-th ROI in $\mathcal{L}^4$ is included in the i-th ROI in $\mathcal{L}^l$. Take Fig. 4 for example. If the ROI R_i^l is composed of the simple nodes R_m^4, R_n^4 and R_t^4 in $\mathcal{L}^4$, the elements of (i,m), (i,n) and (i,t) in $\mathbf{M}^l$ are set to 1, while the others in the i-th row are set to 0. In particular, for the whole brain in $\mathcal{L}^1$, the membership matrix $\mathbf{M}^1$ is a row vector with all N^4 elements set to 1. The following shows that the within-layer and between-layer ROI interactions can be calculated by simply performing some linear operations on the matrix $\mathbf{C}^4$ based on the membership matrix $\mathbf{M}^l$.

Within-layer ROI interaction. Given the ROI interactions in the bottommost layer $\mathcal{L}^4$, the ROI interactions within each of the higher layers are computed as follows. Let R_i^l and R_j^l represent the i-th and j-th ROIs in a certain layer $\mathcal{L}^l$. Again, a matrix $\mathbf{C}^l$ is defined similar to $\mathbf{C}^4$, but its (i,j)-th component now indicates the correlation between the compound ROIs R_i^l and R_j^l. Suppose R_i^l and R_j^l contain a and b simple ROIs respectively. The correlation between R_i^l and R_j^l is computed as the mean value of all the correlations between a simple ROI node from R_i^l and a simple ROI node from R_j^l, that is,

$$corr(R_i^l, R_j^l) = \frac{1}{a \times b} \sum_{R_m^4 \in S_i^l} \sum_{R_n^4 \in S_j^l} corr(R_m^4, R_n^4),$$

where R_m^4 and R_n^4 represent the simple ROIs in $\mathcal{L}^4$, and S_i^l and S_j^l are two sets containing the simple nodes that comprise R_i^l and R_j^l, respectively.

Represented in the form of matrix, the correlation matrix $\mathbf{C}^l$ can be computed as follows:

$$\mathbf{C}^l(i,j) = corr(R_i^l, R_j^l) = \frac{1^{\mathrm{T}} \mathbf{K}_{i,j} * . \mathbf{C}^4 1}{a \times b}, \qquad (1)$$

where $\mathbf{C}^l(i,j)$ denotes the (i,j)-th element in the matrix $\mathbf{C}^l$, the vector 1 is the $N^l \times 1$ vector with all elements equal to 1, the symbol $*.$ represents component-wise product of two matrices, and the $N^4 \times N^4$ matrix $\mathbf{K}_{i,j} = \mathbf{M}^l(i,\cdot)^{\mathrm{T}} \otimes \mathbf{M}^l(j,\cdot)$ is the Kronecker product of the i-th and the j-th rows in the membership matrix $\mathbf{M}^l$.

Between-layer ROI interaction. The correlation matrix that reflects between-layer interactions can be defined similarly to that of within-layer interactions. First, let us consider the correlation matrix for two different layers $\mathcal{L}^{l_1}$ and $\mathcal{L}^{l_2}$ (where $l_1 = 1, 2, 3$; $l_2 = 1, 2, 3$; and $l_1 \neq l_2$). It is defined as:

$$\mathbf{C}^{l_1, l_2}(i,j) = corr(R_i^{l_1}, R_j^{l_2}) = \frac{1^{\mathrm{T}} \mathbf{K}_{(l_1, i),(l_2, j)} * . \mathbf{C}^4 1}{a \times b}, \qquad (2)$$

where $\mathbf{K}_{(l_1, i),(l_2, j)} = \mathbf{M}^{l_1}(i,\cdot)^{\mathrm{T}} \otimes \mathbf{M}^{l_2}(j,\cdot)$ is the Kronecker product of the i-th row in $\mathbf{M}^{l_1}$ and the j-th row in $\mathbf{M}^{l_2}$.

Now, let us consider the correlation matrix for two layers $\mathcal{L}^l$ and $\mathcal{L}^4$. It can be simply computed as:

$$\mathbf{C}^{4,l} = \mathbf{M}^l \mathbf{C}^4 /. \mathbf{H},$$

where $\mathbf{H}$ is an $N^4 \times N^4$ matrix, whose elements in the i-th row are all equal to $\sum_j \mathbf{M}^l(i,j)$, and the symbol $/.$ denotes the component-wise division of two matrices.

Feature vector construction. Note that the hierarchical anatomical brain network may not have the property of small-worldness as shown in DTI and fMRI networks [28,29], because the connections in our case are not based on functions or real
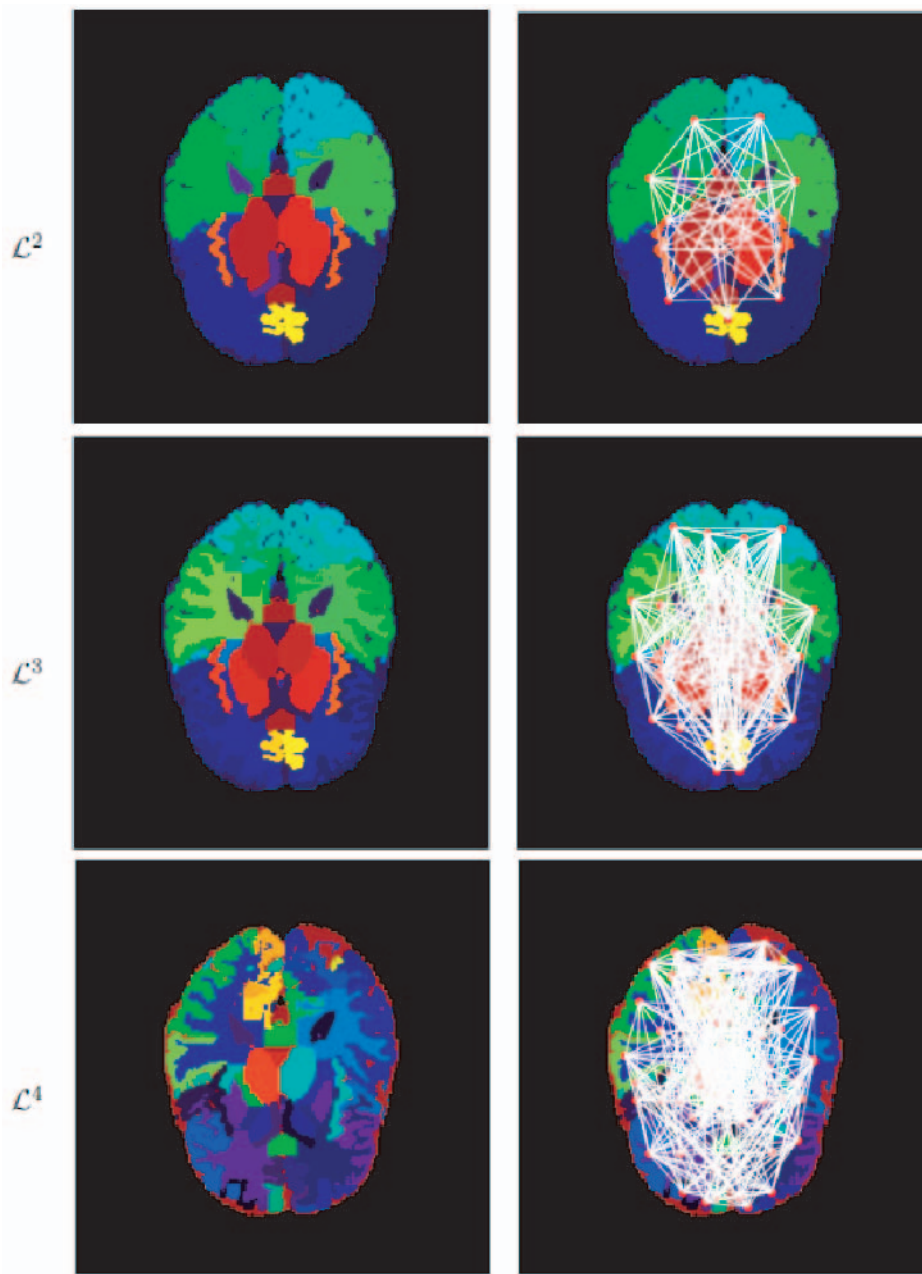
Figure 2. Illustration of hierarchical ROIs. Left: Hierarchical ROIs in three different layers; Right: Network connections between ROIs within different layers.
doi:10.1371/journal.pone.0021935.g002

Table 2. Number of ROIs in the hierarchy.

Layer	Number of ROIs
$\mathcal{L}^1$	1
$\mathcal{L}^2$	20
$\mathcal{L}^3$	44
$\mathcal{L}^4$	100

doi:10.1371/journal.pone.0021935.t002

neuron-connections. Some prior knowledge could be used to prune the edges if it is believed that two ROIs are independent of each other conditioned on the disease. However, in our approach we keep all the connections so that new relationships between structural changes and the disease are not left unexplored. But on the other side, since our network is fully connected, some commonly used network features, such as local clustering coefficients, do not work efficiently as they do for sparse networks in DTI and fMRI. The local clustering coefficient for a node i is computed by averaging its connections to all the other nodes in the network, which might eliminate the necessary discrimination. Therefore, we directly use the weights of edges as features, that is, we concatenate the elements in the upper triangle
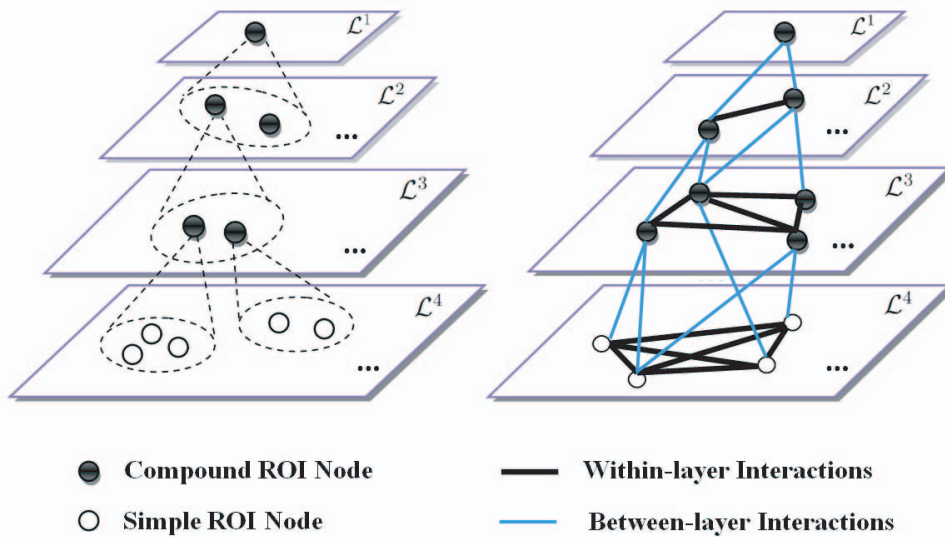
Figure 3. Explanation of the network model. Left: Two types of nodes are included in the hierarchical network: the simple node in $\mathcal{L}^4$, and the compound node in $\mathcal{L}^l (l=1,2,3)$. Each compound node is obtained by grouping several simple nodes agglomeratively. Right: Two types of edges are included in the hierarchical network, each modeling the within-layer and between-layer interactions, respectively.
doi:10.1371/journal.pone.0021935.g003

matrices of correlation matrices computed above. Moreover, before computing the correlation of the volumetric features $\mathbf{f}_i$ and $\mathbf{f}_j$, we employ a normalization step by subtracting $\bar{\mathbf{f}}$ from $\mathbf{f}_i$, where $\bar{\mathbf{f}}$ is the mean volume (in GM, WM, and CSF) of different ROIs belonging to the same subject. By centerizing features in this way, we can obtain a better classification accuracy.
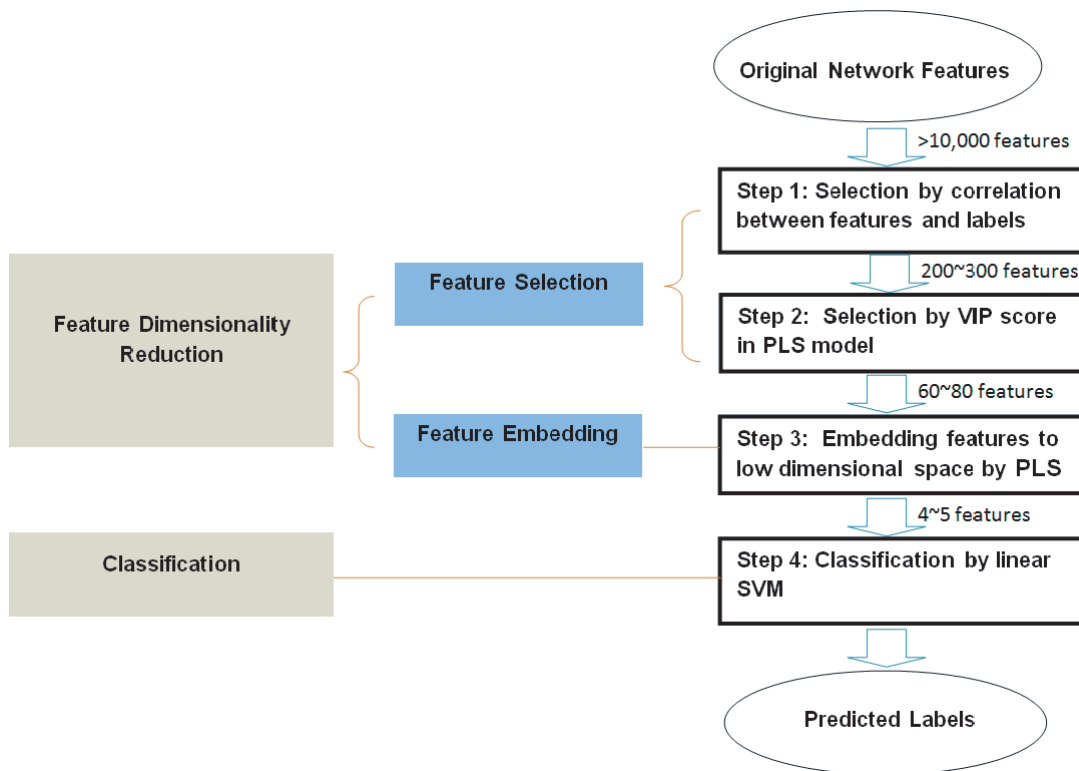
Classification

Since a hierarchical fully-connected brain network is used in our study, the dimensionality of the network features is very high: originally more than 10,000 features for each subject. To address this issue, in this paper, we propose a classification scheme to efficiently learn discriminative information from this large amount of network features. The scheme involves feature dimensionality reduction and classification. The overview of the whole process is given in Fig. 5. As shown, we use both a two-step feature selection (Step 1 and Step 2 in Fig. 5) and a feature embedding (Step 3 in Fig. 5) algorithms to efficiently reduce the dimensionality of features. This gives rise to a small number of discriminative

features that can be well separated by a linear classifier. In particular, the features of the training subjects are first selected according to their relevance with respect to the clinic labels. This step reduces the original more than 10,000 features to about $200 \sim 300$ features. Then in the second step, about $60 \sim 80$ features are further selected based on their predictive power in a Partial Least Square (PLS) model [30]. After the two-step feature selection, another PLS model is trained to embed the selected $60 \sim 80$ features into a low dimensional space that maintains their discriminative power. After feature selection and feature embedding, each subject is represented by only 4 to 5 features. These features are fed into a linear SVM classifier for differentiating MCI patients and normal controls (Step 4 in Fig. 5).

In the rest of this section, our proposed classification scheme is explained in detail. Firstly, in Section "Problem on identifying discriminative features", we justify the necessity of incorporating both feature selection and feature embedding into the dimensionality reduction module in Fig. 5. Then a brief introduction about the Partial Least Square analysis is given in Section "Partial Least
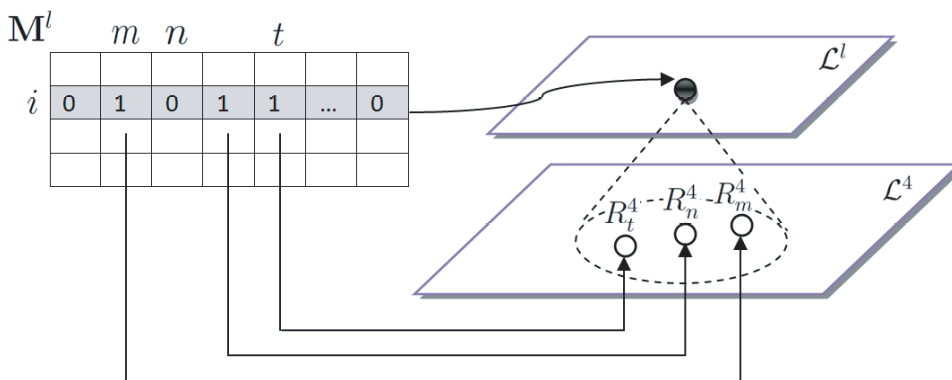
Figure 4. Explanation of the membership matrix. The i-th row in the membership matrix $\mathbf{M}^l$ represents the composition of the node R_i^l in $\mathcal{L}^l$. In our example, since R_i^l is composed of the simple nodes R_m^4, R_n^4 and R_t^4 in $\mathcal{L}^4$, the elements of (i,m), (i,n) and (i,t) in $\mathbf{M}^l$ are set to 1, while the others in the i-th row are set to 0.
doi:10.1371/journal.pone.0021935.g004

Figure 5. Overview of the proposed classification scheme.
doi:10.1371/journal.pone.0021935.g005

Square analysis", which is the key technique used in our classification scheme. PLS integrates the dimensionality reduction process (Step $1 \sim 3$ in Fig. 5) and the classification process (Step 4 in Fig. 5) by considering classification labels when seeking a low dimensional embedding space. It also integrates feature selection (Step 2 in Fig. 5) and feature embedding (Step 3 in Fig. 5) into the same framework to optimize the selection performance. Finally, we summarize how PLS is used to facilitate the classification in our case step by step in Section "Summary of the proposed classification scheme".

Problem on identifying discriminative features. When the number of predefined ROIs is large, the traditional volumetric-based approaches encounter the high feature dimensionality problem. Therefore some preprocessing steps are conducted to reduce the feature dimensionality before classification. There are usually two ways: i) select a subset of the most discriminative features from the original feature set, known as feature selection, or ii) combine the original features linearly or non-linearly to get a lower dimensional feature space, known as feature embedding. Both methods have been reported in the literature. In [4,5], a small subset of features are selected by SVM-Recursive Feature Elimination (SVM-RFE) proposed in [31] and then fed into a nonlinear SVM with a Gaussian kernel. In [32], the volumetric feature vector concatenating the GM, WM and CSF in ROIs are nonlinearly embedded into a lower dimensional feature space by Laplacian Eigenmap, and then a clustering method is used to predict the AD from the normal control.

Compared with volumetric features, the dimensionality of our proposed network features is even much higher. To address this problem, we propose to use both feature selection and feature embedding to efficiently reduce the feature dimensionality. The

reason is two-fold. Firstly, feature selection alone may still give rise to many informative features for the classification. For example, suppose that only 10 ROIs really contribute to the discrimination. The dimension of volumetric features may be maximally reduced to 10 if the feature selection method is effective. However, the number of the corresponding network features that model the pairwise interactions of the 10 ROIs might be up to 45. This possible number is only computed for the layer $\mathcal{L}^4$. If considering about the interactions of ROIs between different hierarchical layers, this number will be further increased. Secondly, feature embedding based on the original high dimensional features may not be able to accurately estimate the underlying data structure due to the existence of too many noisy features. Also, a large amount of features will greatly burden the computation of embedding.

In short, either feature selection or feature embedding *alone* may not be sufficient to identify the discriminative network features with respect to classification. Therefore, a dimensionality reduction process is proposed, which couples feature selection and feature embedding via Partial Least Square (PLS) analysis [30]. As a supervised learning method, PLS considers about the information in the classification labels and thus achieves a better discrimination than many of the commonly used unsupervised methods, for example, Principal Components Analysis (PCA) and the Laplacian Eigenmap. As the key technique used in our classification scheme, a brief introduction about PLS is given to make our paper self-contained.

Partial Least Square analysis. PLS models the relations between the predictive variables (the features $\mathbf{X}$) and the target variables (the labels $\mathbf{Y}$) by means of latent variables. It is often compared to PCA that only models the eigenstructure of $\mathbf{X}$ without considering the relationship between $\mathbf{X}$ and $\mathbf{Y}$. PLS

maximizes the covariance of the projections of **X** and **Y** to latent structures, as well as the individual variance of **X** and **Y**. This method has advantages on data set where the size of the samples is much smaller than the size of the features.

In particular, let the $n \times d$ matrix **X** represent the d-dimensional feature vectors for the n subjects, and **Y** represent the corresponding 1-dimensional label vector. PLS decomposes the zero-mean matrix **X** and the zero-mean vector **Y** into

$$\mathbf{X} = \mathbf{TP}^T + \mathbf{E}$$
$$\mathbf{Y} = \mathbf{UQ}^T + \mathbf{F} \qquad (3)$$

where $\mathbf{T} = (\mathbf{t}_1, \mathbf{t}_2, \cdots, \mathbf{t}_p)$ and $\mathbf{U} = (\mathbf{u}_1, \mathbf{u}_2, \cdots, \mathbf{u}_p)$ are $n \times p$ matrices containing p extracted latent vectors, the $d \times p$ matrix **P** and the $1 \times p$ vector **Q** represent the loadings, and the $n \times d$ matrix **E** and the $n \times 1$ vector **F** are the residuals. The latent matrices **T** and **U** have the following properties: each column of them, called a latent vector, is a linear combination of the original variables **X** and **Y**, respectively; and the covariance of two latent vectors $\mathbf{t}_i$ and $\mathbf{u}_i$ is maximized. PLS can be solved by an iterative deflation scheme. In each iteration, the following optimization problem is solved:

$$[cov(\mathbf{t}_i, \mathbf{u}_i)]^2 = \max_{||\mathbf{w}_i||=1} [cov(\mathbf{Xw}_i, \mathbf{Y})]^2,$$

where **X** and **Y** are deflated by subtracting their rank-one approximations based on $\mathbf{t}_{i-1}$ and $\mathbf{u}_{i-1}$. Once the optimal weight vector $\mathbf{w}_i$ is obtained, the corresponding latent vector $\mathbf{t}_i$ can be computed by $\mathbf{t}_i = \mathbf{Xw}_i$. For more details, please see [30].

Summary of the proposed classification scheme. Taking advantages of PLS analysis, our proposed method achieves good classification and generalization in four steps, as shown in Fig. 5.

In Step 1, the discriminative power of a feature is measured by its relevance to classification. The relevance is computed by Pearson correlation between each original feature and the classification label. The larger the absolute value of the correlation, the more discriminative the feature. Features with correlation values lower than a threshold are filtered out.

In Step 2, a subset of features are further selected from the result of Step 1 in order to optimize the performance of PLS embedding in Step 3. In particular, a PLS model is trained using the selected features from Step 1. Then a method called Variable Importance on Projection (VIP) [33] is used to rank these features according to their discriminative power in the learned PLS model. The discriminative power is measured by a VIP score. The higher the score, the more discriminative the feature. A VIP score for the j-th feature is

$$VIP_j = \sqrt{\frac{d \sum_{k=1}^{p} \rho_k^2 w_{jk}^2}{\sum_{k=1}^{p} \rho_k^2}},$$

where d is the number of features, p is the number of the latent vectors as defined above, w_{jk} is the j-th element in the vector $\mathbf{w}_k$, and ρ_k is the regression weight for the k-th latent variable, that is, $\rho_k = \mathbf{u}_k^T \mathbf{t}_k$. About $60 \sim 80$ features with the top VIP scores are selected for feature embedding in the next step.

In Step 3, using the features selected in Step 2, a new PLS model is trained to find an embedding space which best preserves the discrimination of features. The embedding is performed by projecting the feature vectors in the matrix **X** onto the new weight vectors $\mathbf{W} = (\mathbf{w}_1, \mathbf{w}_2, \cdots, \mathbf{w}_p)$ learned by PLS analysis. In other words, the representation of each subject changes from a

row in the feature matrix **X** to a row in the latent matrix **T**. The feature dimensionality is therefore reduced from d to p ($p \ll d$).

In Step 4, after PLS embedding, a small number of features in the new space are able to capture the majority of the class discrimination. This greatly reduces the complexity of relationships between data. Therefore, these features are used to train a linear SVM for predicting MCI patients and normal controls. In our case, a linear SVM can achieve better or at least comparable classification accuracies as a non-linear SVM.

The advantages of PLS for our network features over some commonly used unsupervised and supervised nonlinear methods, such as Laplacian eigenmap embedding and Kernel Fisher Discriminant Analysis (KFDA), have been evidently shown in our experiment in Section "Comparison of Classifiers".

Results and Discussion

In our study, we conduct two kinds of comparisons, that is, to compare the discrimination power of the network and the volumetric features, and to compare the performance of different classifiers for the network features. The discussion of the classification results are given at the end of this section.

Please note that, as MCI patients are highly heterogeneous, the comparison of the absolute classification accuracy with the existing works in the literature is meaningless. Therefore in our study, we evaluate the improvement of our proposed approach over the conventional volumetric features by comparisons on the same data set with the same experiment configuration. Furthermore, to investigate the generalization of the proposed method, we conduct experiments repetitively on different random partitions of training and test data sets with different partition ratios. The average classification accuracy estimated in this way tends to be more conservative than the traditional Leave-One-Out approach. More discussions are given below.

Comparison of Features

Firstly, we compare the efficacy of different features with respect to classification. The data set is randomly partitioned into 20 training and test groups with 75 samples for training and 75 samples for test. For a fair comparison, our proposed classification process is applied similarly to both the volumetric and the network features.

As aforementioned, our network features differ from the conventional volumetric features in two aspects: i) the network features model the regional interactions; ii) the network features are obtained from a four-layer hierarchy of brain atlases. The contributions of these two aspects are investigated separately. To test the advantages of using regional interactions over local volumes, we compare the network and the volumetric features on the same hierarchical structure (either single-layer or four-layer). To test the advantages of using the hierarchical network structure, we compare network features obtained from different layers (the bottommost layer and all four layers) in the hierarchy. Moreover, we compare the networks with and without the cross-layer connections to further explore the function of the hierarchial structure. In summary, five methods are tested in the experiment:

- Method I is the proposed method in this paper, using the four-layer hierarchical network features.
- Method II only uses the network features from the bottommost layer $\mathcal{L}^4$. It tests the classification performance of network features on a single layer.
- Method III uses the network features from all the four layers, but removing the edges across different layers. It tests how the

cross-layer connections in the hierarchy contribute to the classification.

- Method IV uses the volumetric features (the concatenation of GM, WM and CSF ratios in the ROIs) from the bottommost layer $\mathcal{L}^4$. It corresponds to the conventional volume-based method.

- Method V uses volumetric measures from all four layers. It tests if the volumetric features obtained from the hierarchy can achieve similar classification performance as the hierarchical network features.

The results are summarized in Table 3. The classification accuracy in Table 3 is averaged across the 20 randomly partitioned training and test groups. A paired t-test is conducted between Method I and the other four methods respectively, to demonstrate the advantage of our proposed method. The t-value and the corresponding p-value of the paired t-test are also reported. It can be seen from Table 3 that Method I is always statistically better (the significance level 0.05) than any of the other four methods. In addition to comparing the average accuracies in Table 3, the classification accuracies are also compared on each of the 20 training-test groups between the four-layer network features (Method I) and the conventional volume features (Method IV) in Fig. 6, and between the four-layer network features (Method I) and the single-layer network features (Method II) in Fig. 7.

Combining the results from Table 3, Fig. 6 and Fig. 7, we observe the following:

- Our proposed hierarchical network features in Method I outperform the conventional volumetric features in Method IV. The advantage may come from using both regional interactions and the hierarchical structure.

- To demonstrate the benefit purely from using the regional interactions, the same atlases in the hierarchy are applied to volumetric features as in Method V. It can be seen from Table 3 that the hierarchical structure does not improve the discrimination of the single-layer volumetric features in Method IV. Moreover, the benefit of using regional interactions can also be shown by the better result of the single-layer network features in Method II than the single-layer volumetric features in Method IV.

- To demonstrate the benefit purely from the hierarchy, we compare the classification performance of the single-layer network features in Method II and the four-layer network features in Method I. The advantage of the four-layer structure is statistically significant over the single-layer. Moreover, the result that Method I statistically outperforms Method III indicates the necessity of using the cross-layer edges in the network.

Table 3. Comparison of discrimination efficacy of different features.

	Mean Test Accuracy (%)	Paired t-test	
		t-value	p-value
Method I	85.07 ± 3.92	-	-
Method II	83.0 ± 3.65	3.1349	0.00272
Method III	83.13 ± 3.43	3.0009	0.00367
Method IV	81.93 ± 3.76	3.3558	0.00166
Method V	81.47 ± 3.95	4.4163	0.00015

It is noticed that different ratios of training and test partitions may lead to a variation in the classification accuracy. To reflect the influence of this factor, we test seven different numbers of training samples, occupying 50% to 80% of the total data size. For each number of training samples, 20 training and test groups are randomly generated and the average classification accuracy is summarized in Fig. 8. When 150 training samples are used, the test accuracy in Fig. 8 corresponds to the classification accuracy of 85.07% obtained by Method I in Table 3. In general, the classification accuracy goes up slightly when the number of the training samples increases. This is not surprising because the larger the number of training samples, the more the learned information. It can be seen that the network features show a consistent improvement in classification accuracy of approximately 3% in all cases, compared to those by using the conventional volumetric features. Averaged across different numbers of training samples, the classification accuracy becomes 84.35% for the network features, and 80.83% for the volumetric features, which represents an overall classification performance of these two different features. A paired t-test is performed on the seven different ratios of training-test partitions using both features. The obtained p-value of 0.000024 indicates that the improvement of the network features over the volumetric features is statistically significant.

It is worth noting that the influence of different ratios of training-test partitions on the classification result is often ignored in many existing works. One possible reason is that a Leave-One-Out validation is used when the size of the data is small. This often leads to the use of more than 90% data for training, which tends to produce a more optimistic result compared with using other lower ratios of training data.

Comparison of Classifiers

The classification performance of our proposed classification scheme is compared with other six possible schemes shown in Table 4. To simplify the description, our proposed scheme is denoted as P1, while the other six schemes in comparison are denoted as P2∼P7. To keep consistent with P1, each of the six schemes P2∼P7 is also divided into four steps: rough feature selection, refined feature selection, feature embedding and classification, corresponding to Step 1∼Step 4 in P1. Please note that the first step, rough feature selection, is the same for all schemes P1∼P7. In this step, the discriminative features are selected by their correlations with respect to the classification labels. From the second step onwards, different schemes utilize different configurations of strategies, as shown in the second column of Table 4.
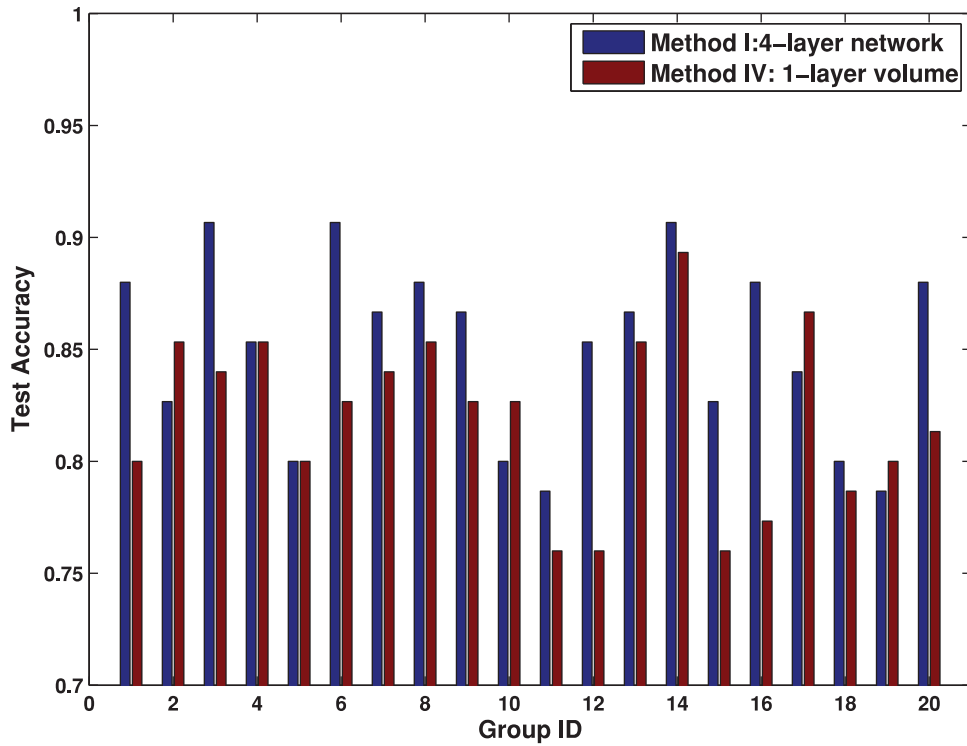
To clarify the settings of our experiment, the Laplacian embedding used in P7 is described as follows. The embedding is applied on a connection graph that shows the neighboring relationship of the subjects. Based on the connection graph, the distance between two subjects is computed as the shortest distance between the corresponding two nodes in the graph. This distance is used to construct the adjacent matrix and Laplacian matrix used in the Laplacian embedding. The Laplacian embedding in our experiment is different from the one in [32] where the distance between two subject is computed based on the deformation estimated by the registration algorithm.

The classification results are summarized in Fig. 9 and Table 4. Please note that the classification accuracy at each number of training samples in Fig. 9 is an average over 20 random training and test partitions as mentioned in Section "Comparison of Features". Also, the overall classification accuracy in Table 4 is an average of accuracies at different numbers of training samples in Fig. 9. The best overall classification accuracy of 84.35% is obtained by our proposed scheme P1: VIP selection + PLS
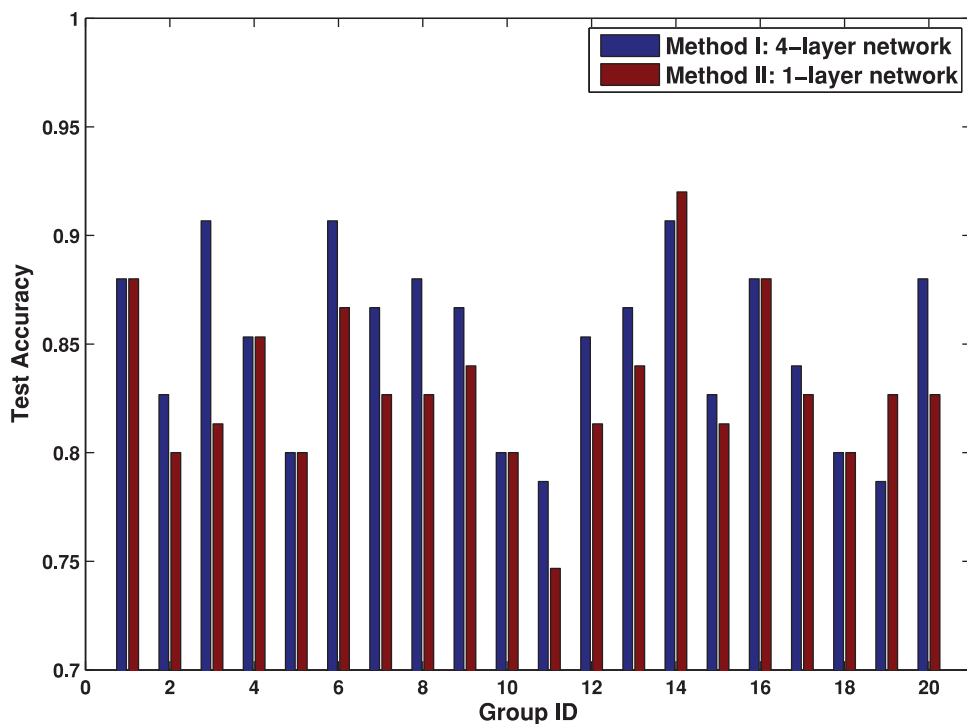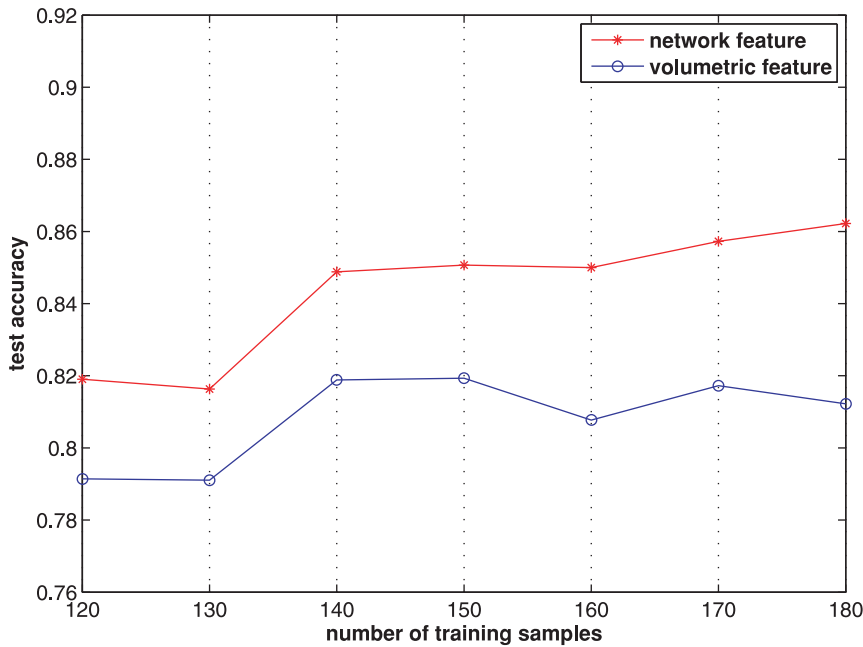
Figure 6. Classification comparison using different features. The classification performance is compared between our proposed method (four-layer network features as in Method I) and the conventional volumetric method (Method IV) on 20 training/test groups. Each group contains 150 training samples and 75 test samples randomly partitioned from our data set.
doi:10.1371/journal.pone.0021935.g006

Figure 7. Classification comparison using different hierarchical structure. The classification performance is compared between the four-layer network features in Method I and the single layer network features in Method II on 20 training/test groups. Each group contains 150 training samples and 75 test samples randomly partitioned from our data set.
doi:10.1371/journal.pone.0021935.g007

Figure 8. Classification comparison using network features and volumetric features with different numbers of training samples.
doi:10.1371/journal.pone.0021935.g008

embedding + a linear SVM. This is slightly better than P2, where a nonlinear SVM is used. It can be seen that the classification schemes with PLS embedding (P1 ∼ P4) achieve an overall accuracy above 84%, better than those without PLS embedding (P5 ∼ P7). The supervised embedding methods, i.e., PLS (P1 ∼ P4) and KFDA (P7), perform better than the unsupervised Laplacian Eigenmap embedding (P6). Moreover, PLS embedding (P1 ∼ P4) preserves more discrimination than the nonlinear supervised embedding of KFDA (P7).

Although the proposed scheme P1 achieves the best classification performance, the difference between P1 ∼ P4 is not significant. This may indicate that the discriminative dimensionality reduction by PLS embedding plays a more important role than the classifier type in improving classification performance. After PLS embedding, the data complexity is greatly reduced and the intrinsic relationship underlying the data becomes more evident, therefore allowing even simple classifiers to achieve performance comparable to more sophisticated classifiers. Although the difference between P1 ∼ P4 is not significant, P1 is still preferred over P2 and P4 because the linear SVM employed in P1 is much faster than the nonlinear SVM employed in P2 and P4. P1 is also preferred over P3, because the

VIP selection employed in P1, while yielding improvement over P3, does not increase the computational cost substantially.

Spatial Patterns

Note that each network feature characterizes the relationship between two ROIs, instead of an individual ROI as in the conventional approaches. Therefore, for the first time, we study the *relative* progression speed of the disease in different ROIs of the same subject, which eliminates the impact of personal variations. On the contrary, the conventional methods study the *absolute* progression speeds of ROIs among different subjects. Normalizing subjects by the whole brain volume in conventional methods may not completely remove the personal variations.

To be an essentially discriminative network feature, the two associated ROIs may satisfy one of the two following conditions:

- One ROI shows significant difference between the MCI group and the normal control group, while the other ROI is relatively constant with respect to the disease. Therefore the correlation between these two ROIs varies over the two groups in comparison.

Table 4. Configurations of classification Schemes.

Schemes	Configurations	classification accuracy overall (%)
P1	VIP selection + PLS embedding + linear SVM	84.35
P2	VIP selection + PLS embedding + nonlinear SVM	84.03
P3	no selection + PLS embedding + linear SVM	84.11
P4	no selection + PLS embedding + nonlinear SVM	84.10
P5	SVM-RFE selection + no embedding + nonlinear SVM	80.07
P6	no selection + Laplacian Eigenmap embedding + nonlinear SVM	79.16
P7	no selection + KFDA embedding + linear SVM	81.08

doi:10.1371/journal.pone.0021935.t004
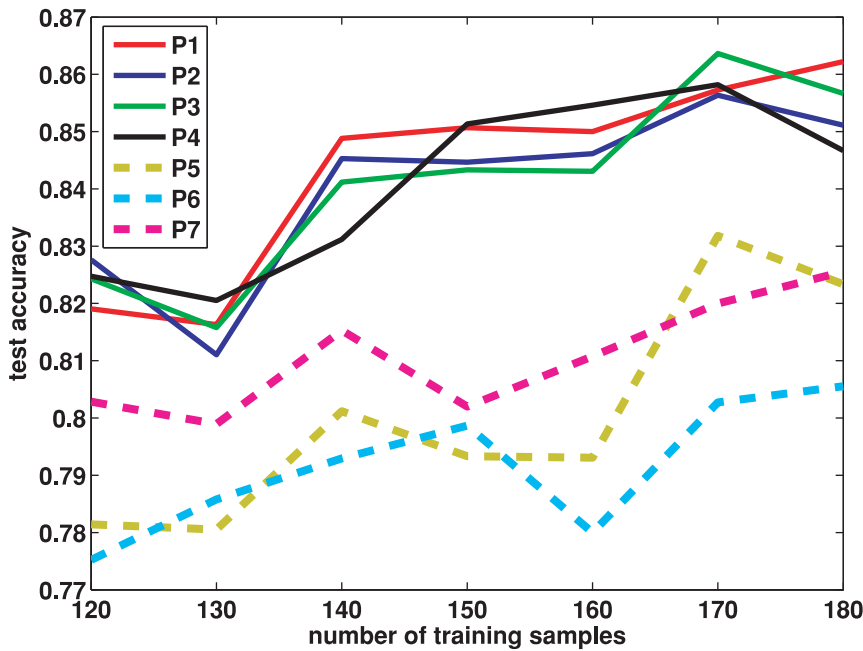
Figure 9. Comparison of seven classification schemes on network features. The classification accuracy is plotted over different number of training samples. For a given number of training samples, the classification accuracy is averaged over 20 training/test groups randomly partitioned from our data set using this number of training samples. The scheme configurations are shown in Table 4.
doi:10.1371/journal.pone.0021935.g009

- Both ROIs change with the disease, but their change speeds are different over two different groups.

The selected features are different for the twenty randomly partitioned training and test groups used in Section "Comparison of Features". Table 5 shows the most discriminative features selected by more than half of the training and test groups. It can be clearly seen that hippocampus remains the most discriminative ROI in differentiating the normal controls and MCI patients. Table 5 is separated into two parts. On the upper portion of the table, the two ROIs of a network feature may be both associated with the MCI diagnosis, such as hippocampus, entorhinal cortex, uncus, fornix, globus palladus, cingulate etc, as reported in the literature [4,5,7,10,13,15,19,20,34,35]. A typical example is the correlation

between hippocampus and ventricle. It is known that the enlargement of ventricle is a biomarker for the diagnosis of the AD [36]. However, different from the hippocampus volume loss that often occurs at the very early stage of the dementia, the ventricle enlargement often appears in the middle and late stages. Therefore, the progression pattern of disease in these two regions is different. Their correlation is thus selected as the discriminative feature. On the lower portion of the table, the first ROI is associated with the disease, while the second ROI is not. For example, it has been reported that the anterior and posterior limbs of internal capsule and the occipital lobe white matter are not significantly different between MCI patients and normal controls in a DTI study [37].

Metrics

In our network design, each edge represents the correlation or the "similarity" between a pair of ROI nodes. Pearson correlation is just one of the possible similarity measurements. By viewing Pearson correlation as an inverse distance, it is straightforward to include other commonly used distance metrics, e.g., the Euclidean distance, the $L1$-norm distance, and the kernel based distance, for measuring the feature similarity between ROI pairs. By virtue of separating the computation of the hierarchy and the regional interactions, our proposed method can be easily generalized to other metrics with merely a slight revision of (1) and (2) as follows. The within-layer interaction is computed as

$$\mathbf{D}^l(i,j) = \frac{1^\mathrm{T}\mathbf{K}_{i,j} * .\mathbf{D}^4 1}{a \times b}, \qquad (4)$$

and the between-layer interaction is computed as

$$\mathbf{D}^{l_1,l_2}(i,j) = \frac{1^\mathrm{T}\mathbf{K}_{(l_1,i),(l_2,j)} * .\mathbf{D}^4 1}{a \times b}, \qquad (5)$$

Table 5. Selected discriminative features.

hippocampus – amygdala
hippocampus - lingual gyrus
hippocampus – uncus
hippocampus - prefrontal/superolateral frontal lobe
hippocampus - globus palladus
hippocampus - entorhinal cortex
hippocampus - cingulate region
hippocampus – ventricle
hippocampus and amygdala and fornix – ventricle
uncus – fornix
hippocampus - posterior limb of internal capsule
globus palladus - anterior limb of internal capsule
hippocampus - occipital lobe WM

doi:10.1371/journal.pone.0021935.t005

Table 6. Comparison of different metrics for modeling the regional interactions.

	Mean Test Accuracy (%)
Euclidean	82.27
L1	80.07
Kernel	84.47
Pearson Correlation	85.07
Volumetric	81.93

doi:10.1371/journal.pone.0021935.t006

where $\mathbf{D}^4$ is a general metric that measures the relationship between two ROIs in the bottommost layer $\mathcal{L}^4$. The definitions of other symbols remain the same. If Pearson correlation is used, these two equations become identical to (1) and (2). It can be seen that, for a different metric, the hierarchy can be left intact and only the regional interactions in the bottommost layer need to be recomputed.

Using (4) and (5), we test the performance of the three alternative metrics: the Euclidean distance $\mathbf{D}^4_{L2}(i,j)$, the $L1$-norm distance $\mathbf{D}^4_{L1}(i,j)$, and the kernel based distance $\mathbf{D}^4_{ker}(i,j)$. They are defined as follows:

$$\mathbf{D}^4_{L2}(i,j) = \sqrt{\sum_{k=1}^{3}(\mathbf{f}_{ik}-\mathbf{f}_{jk})^2},$$

$$\mathbf{D}^4_{L1}(i,j) = \sum_{k=1}^{3}|\mathbf{f}_{ik}-\mathbf{f}_{jk}|, \qquad (6)$$

$$\mathbf{D}^4_{ker}(i,j) = \exp-\frac{\|(\mathbf{f}_i-\mathbf{f}_j)\|^2}{2\sigma^2}.$$

The Euclidean distance and the $L1$-norm distance measure the linear relationship between a pair of ROI nodes. No parameter needs to be set. The kernel based distance provides a non-linear measurement of ROI feature similarity. The parameter σ is set, by cross-validation, to be 0.2 times the average Euclidean distance between ROI pairs. Based on the 20 random training and test partitions as in Section "Comparison of Features", the average classification accuracies are reported in Table 6. For comparison, the accuracies of our network approach using Pearson correlation, and the conventional volumetric approach are also repeated in the table. In addition, the test accuracies over different numbers of training samples for different metrics are plotted in Fig. 10. It can be seen that, Pearson correlation yields the best performance, followed by the kernel based distance. These two distances give significant improvement over the conventional volumetric approach, whereas the Euclidean and the $L1$-norm distances do not. The importance of the choice of the metric is quite visible: only when a proper metric is selected, the network construction may bring useful information compared with the conventional volumetric approach.

Conclusion

In this paper, we have presented how hierarchical anatomical brain networks based on T1-weighted MRI can be used to model brain regional correlation. Features extracted from these networks are employed to improve the prediction of MCI from the conventional volumetric measures. The experiments show that, without requiring new sources of information, the improvement brought forth by our proposed approach is statistically significant compared with conventional volumetric measurements. Both the network features and the hierarchical structure contribute to the improvement. Moreover, the selected network features provide us a new perspective of inspecting the discriminative regions of the dementia by revealing the relationship of two ROIs, which is
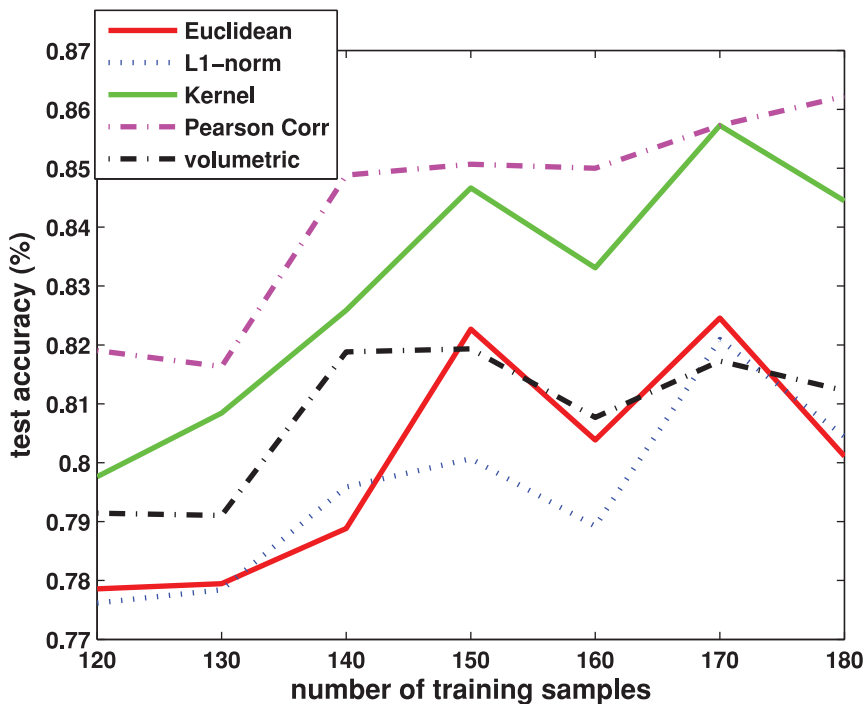
Figure 10. Comparison of different metrics used for modeling the regional interactions. The classification accuracy is plotted over different number of training samples. For a given number of training samples, the classification accuracy is averaged over 20 training/test groups randomly partitioned from our data set using this number of training samples.
doi:10.1371/journal.pone.0021935.g010

different from the conventional approaches. The flexibility to generalize our proposed method has been demonstrated by different distance metrics tested in our experiment.

Acknowledgments

Author Contributions

Conceived and designed the experiments: LZ DS YL P-TY. Performed the experiments: LZ. Analyzed the data: LZ. Contributed reagents/materials/analysis tools: YW. Wrote the paper: LZ YL P-TY DS.

References

1. Chételat G, Baron J (2003) Early diagnosis of alzheimer's disease: contribution of structural neuroimaging. Neuroimage 18: 525–541.
2. Jack Jr. C, Petersen R, Xu Y, Waring S, O'Brien P, et al. (1997) Medial temporal atrophy on mri in normal aging and very mild alzheimer's disease. Neurology 49: 786–794.
3. Jack Jr. C, Petersen R, Xu Y, O'Brien P, Smith G, et al. (1998) Rate of medial temporal lobe atrophy in typical aging and alzheimer's disease. Neurology 51: 993–999.
4. Fan Y, Shen D, Davatzikos C (2005) Classification of structural images via highdimensional image warping, robust feature extraction, and svm. In: Proceedings of the 8th International Conference on Medical Image Computing and Computer-Assisted Intervention. pp 1–8.
5. Fan Y, Shen D, Gur R, Davatzikosa C (2007) Compare: classification of morphological patterns using adaptive regional elements. IEEE Trans Med Imaging 26: 93–105.
6. Fan Y, Batmanghelich N, Clark C, Davatzikos C, Initiative ADN (2008) Spatial patterns of brain atrophy in mci patients, identified via high-dimensional pattern classification, predict subsequent cognitive decline. Neuroimage 39: 1731–1743.
7. Fan Y, Resnick S, Wu X, Davatzikos C (2008) Structural and functional biomarkers of prodromal alzheimer's disease: a high-dimensional pattern classification study. Neuroimage 41: 277–285.
8. Thompson P, Mega M, Woods R, Zoumalan C, Lindshield C, et al. (2001) Cortical change in alzheimer's disease detected with a disease-specific population-based brain atlas. Cereb Cortex 1: 1–16.
9. Thompson P, Hayashi K, de Zubicaray G, Janke A, Rose S, et al. (2003) Dynamics of gray matter loss in alzheimer's disease. Journal of Neuroscience 23: 994–1005.
10. Thompson P, Hayashi K, Sowell E, Gogtay N, Giedd J, et al. (2004) Mapping cortical change in alzheimer's disease, brain development, and schizophrenia. Journal of Neuroscience 23: S2–S18.
11. Dickerson B, Bakkour A, Salat D, Feczko E, Pacheco J, et al. (2009) The cortical signature of alzheimer's disease: regionally specific cortical thinning relates to symptom severity in very mild to mild ad dementia and is detectable in asymptomatic amyloid-positive individuals. Cereb Cortex 19: 497–510.
12. Lerch J, Pruessner J, Zijdenbos A, Collins D, Teipel S, et al. (2008) Automated cortical thickness measurements from mri can accurately separate alzheimer's patients from normal elderly controls. Neurobiol Aging 29: 23–30.
13. Convit A, De Leon M, Tarshish C, De Santi S, Tsui W, et al. (1997) Specific hippocampal volume reductions in individuals at risk for alzheimer's disease. Neurobiol Aging 18: 131–138.
14. Colliot O, Chtelat G, Chupin M, Desgranges B, Magnin B, et al. (2008) Discrimination between alzheimer disease, mild cognitive impairment, and normal aging by using automated segmentation of the hippocampus. Radiology 248: 194–201.
15. Chupin M, G'erardin E, Cuingnet R, Boutet C, Lemieux L, et al. (2009) Fully automatic hippocampus segmentation and classification in alzheimer's disease and mild cognitive impairment applied on data from adni. Hippocampus 19: 579–587.
16. Klöppel S, Stonnington C, Chu C, Draganski B, Scahill R, et al. (2008) Automatic classification of mr scans in alzheimer's disease. Brain 131: 681–689.
17. Lao Z, Shen D, Xue Z, Karacali B, Resnick S, et al. (2004) Morphological classification of brains via high-dimensional shape transformations and machine learning methods. Neurobiol Aging 21: 46–57.
18. Magnin B, Mesrob L, Kinkingnhun S, Plgrini-Issac M, Colliot O, et al. (2009) Support vector machine-based classification of alzheimer's disease from whole-brain anatomical mri. Neuroradiology 51: 939–944.
19. Braak H, Braak E (1995) Staging of alzheimer's disease-related neurofibrillary changes. Neurobiol Aging 16: 271–278.
20. Cuingnet R, Gerardin E, Tessieras J, Auzias G, Lehricy S, et al. (2010) Automatic classification of patients with alzheimer's disease from structural mri: A comparison of ten methods using the adni database. Neuroimage 56: 766–781.
21. Davatzikos C, Fan Y, Wu X, Shen D, Resnick S (2008) Detection of prodromal alzheimer's disease via pattern classification of magnetic resonance imaging. Neurobiol Aging 29: 514–523.
22. Zhou L, Wang Y, Li Y, Yap P, Shen D, et al. (2011) Hierarchical anatomical brain networks for mci prediction by partial least square analysis. In: Proceedings of Computer Vision and Pattern Recognition 2011 (to appear).
23. Jack Jr. C, Bernstein M, Fox N, Thompson P, Alexander G, et al. (2008) The alzheimer's disease neuroimaging initiative (adni): Mri methods. J Magn Reson Imaging 27: 685–691.
24. McKhann G, Drachman D, Folstein M, Katzman R, Price D, et al. (1984) Clinical diagnosis of alzheimer's disease: report of the nincds-adrda work group under the auspices of department of health and human services task force on alzheimer's disease. Neurology 34: 939–944.
25. Sled J, Zijdenbos A, Evans A (1998) A nonparametric method for automatic correction of intensity nonuniformity in mri data. IEEE Trans Medical Imaging 17: 87–97.
26. Shen D, Davatzikos C (2003) Very high resolution morphometry using mass-preserving deformations and hammer elastic registration. NeuroImage 18: 28–41.
27. Kabani N, MacDonald J, Holmes C, Evans A (1998) A 3d atlas of the human brain. NeuroImage 7: S7–S17.
28. Bassett D, Bullmore E (2006) Small-world brain networks. Neuroscientist 12: 512–523.
29. Achard S, Salvador R, Whitcher B, Suckling J, Bullmore E (2006) A resilient, lowfrequency, smallworld human brain functional network with highly connected association cortical hubs. Journal of Neuroscience 26: 63–72.
30. Rosipal R, Kramer N (2006) Overview and recent advances in partial least squares. Lecture Notes in Computer Science 3940: 34–51.
31. Guyon I, Weston J, Barnhill S, Vapnik V (2002) Gene selection for cancer classification using support vector machines. Machine Learning 46: 389–422.
32. Long X, Wyatt C (2010) An automatic unsupervised classification of mr images in alzheimers disease. In: Proceedings of Computer Vision and Pattern Recognition 2010.
33. Wold S, Johansson W, Cocchi M (1993) Pls - partial least- squares projections to latent structures. 3D QSAR in Drug Design: Volume 1: Theory Methods and Applications 1: 523–550.
34. Pengas G, Hodges J, Watson P, Nestor P (2010) Focal posterior cingulate atrophy in incipient alzheimer's disease. Neurobiol Aging 31: 25–33.
35. Copenhaver B, Rabin L, Saykin A, Roth R, Wishart H, et al. (2006) The fornix and mammillary bodies in older adults with alzheimer's disease, mild cognitive impairment, and cognitive complaints: a volumetric mri study. Psychiatry Res 147: 93–103.
36. Nestor S, Rupsingh R, Borrie M, Smith M, Accomazzi V, et al. (2008) Ventricular enlargement as a possible measure of alzheimer's disease progression validated using the alzheimer's disease neuroimaging initiative database. Brain 131: 2443–2454.
37. Bozzali M, Falini A, Franceschi M, Cercignani1 M, Zuffi M, et al. (2002) White matter damage in alzheimer's disease assessed in vivo using diffusion tensor magnetic resonance imaging. Journal of Neurol Neurosurg Psychiatry 72: 742–746.